Microscopic Modeling of HfO$_x$ RRAM Operations: From Forming to Switching

Andrea Padovani, *Member, IEEE*, Luca Larcher, *Member, IEEE*, Onofrio Pirrotta,
Luca Vandelli, and Gennadi Bersuker, *Member, IEEE*

Abstract—We propose a model describing the operations of hafnium oxide-based resistive random access memory (RRAM) devices at the microscopic level. Charge carrier and ion transport are self-consistently described starting from the leakage current in pristine HfO$_2$. Material structural modifications occurring during the RRAM operations, such as conductive filament (CF) creation and disruption, are accounted for. The model describes the complex processes leading to a formation of the CF and its dependence on both electrical conditions (e.g., current compliance, voltage stress, and temperature) and device characteristics (e.g., electrodes material and dielectric thickness).

Index Terms—Conductive filament (CF), forming, HfO$_2$, RESET, resistive random access memory (RRAM), resistive switching, SET, trap-assisted tunneling (TAT).

I. INTRODUCTION

RESISTIVE random access memories (RRAMs) based on transition metal oxides are one of the most promising options for ultrascaled nonvolatile memory devices for both embedded and high-density applications [1]. Among the variety of technologies and materials proposed so far, the RRAM devices based on hafnium oxide showed very promising characteristics: short switching times (~1 ns), good endurance (>10^{12}) and retention, compatibility to the CMOS manufacturing process, and a very simple structure [1], [2].

An initial operation, called forming, is usually required for some types of the RRAM devices to establish a conductive filament (CF) connecting the top and bottom MIM electrodes. The CF is formed through a process similar to a dielectric breakdown: the applied voltage leads to bond breakage and formation of a metal-rich region connecting the top and bottom electrodes. A current compliance limit may be imposed to control filament cross section and switching current [1]. Once the CF is formed, the resistance of the HfO$_x$ layer can be switched between a low-resistance state (LRS) and

a high-resistance state (HRS) by applying voltage pulses of opposite polarities [1].

The forming process is a critical step for the operation of the RRAM devices [3], as it determines the CF characteristics (e.g., shape, radius, and atomic configuration) that affect the subsequent RRAM performance and reliability (CF stability, SET and RESET voltages, retention, and endurance). Thus, a comprehensive understanding of the RRAM operation requires linking the microscopic properties of the filament to the device electrical characteristics.

From the modeling perspective, a comprehensive description of the RRAM operations allows removing some arbitrary assumptions (e.g., the CF characteristics) typically considered in reported RRAM models, which are primarily focused on the switching (RESET and SET) operations [4]–[9]. Such models employ a variety of approaches and methodologies, such as percolation-based theories [5], [7], [8], metal ions migration mechanism [4], quantum point contact theory [6], and kinetic Monte Carlo (kMC) approach [9]. They frequently rely on a phenomenological-statistical description considering only a limited set of the physical processes contributing to the RRAM device operations. This may lead to an oversimplified descriptions that works effectively only for specific devices under the used operation conditions and may be not applicable when they are modified. Moreover, the geometrical and physical characteristics of the CF, crucial for understanding the RRAM functionality, are typically postulated rather than being derived in the framework of a unified and self-consistent approach.

In this paper, we present a physical model describing at the microscopic level, the operations of HfO$_x$ RRAM devices starting from the creation of a conductive (Hf-rich) filament occurring during the forming processes [10]–[12]. The model describes the transport of charge carriers and ions and the material structural modifications associated with the RRAM operations. The charge transport is described in the framework of the multiphonon trap-assisted tunneling (TAT) [13], [14] via structural defects (oxygen vacancies) in the dielectric [14], [15]. The power dissipation and temperature increase associated with the current are included, and the temperature-field induced generation, recombination, and drift/diffusion (DD) of oxygen vacancy/ion pairs are described statistically through a kMC approach [11], [12]. This enables simulating current–voltage characteristics (and their statistics) during

forming/SET/RESET processes and provides quantitative understanding of the kinetics of the physical processes governing the RRAM operations.

This paper is organized as follows. The implications of the HfO$_2$ microscopic properties on the charge transport and the RRAM operations are discussed in Section II. The physical model for the simulation of the RRAM operations is presented in Section III. The dynamic of the forming process and the effect of the forming conditions (i.e., temperature, voltage stress, and current compliance) are shown in Sections IV and V, respectively. SET and RESET simulations are described in Section VI.

II. IMPLICATIONS OF MICROSCOPIC HfO$_2$ PROPERTIES ON CHARGE TRANSPORT AND RRAM OPERATIONS

Atomic characteristics of the HfO$_2$ structure strongly affect the RRAM operations and have thus to be explicitly considered in order to develop a predictive physical model connecting device electrical characteristics to its material properties.

In polycrystalline HfO$_2$ dielectrics, grain boundaries (GBs) play a crucial role in the charge transport and the structural modifications occurring during the RRAM operation [16]–[19]. Ab-initio calculations and conductive atomic force microscopy measurements indicate that positively charged oxygen vacancies accumulate in the GBs, while oxygen ions are energetically driven to diffuse out of the GB sites [16], [17]. Since the transport of electrons can effectively proceed via the oxygen vacancies, the GBs represent the preferential paths for the electron transfer through the dielectric [16], [19], [20]. Furthermore, positive oxygen vacancies can also contribute to keep oxygen ions confined during switching, thus improving the RRAM device endurance and retention [21].

The HfO$_2$ stoichiometry is another material characteristic strongly affecting the charge transport and the RRAM device operation. Increasing the pristine O vacancy density increases the leakage current, reduces the forming voltage [15], [22] and is necessary to ensure reliable switching [23]. The dielectric stoichiometry can be manipulated through an active metal film (e.g., Ti) located next to the dielectric surface, the so-called oxygen exchange layer (OEL), which getters oxygen from the underling HfO$_x$ [23], [24]. The oxygen out-diffusion driven by this active metal layer leads to the formation of a metal suboxide (e.g., TiO$_y$) at the OEL/HfO$_x$ interface, which plays an important role in the SET/RESET operations [23]. The thickness of this layer is reported to vary after forming and switching, indicating that the RRAM operations could involve the exchange of oxygen ions between the HfO$_x$ and the OEL [23]. All the above features, strongly connected to the material, are included in the model described in Section III.

III. RRAM DEVICE MODEL

The physical model that we developed connects the electrical device characteristics to the material properties. The model is comprised of several modules describing the main
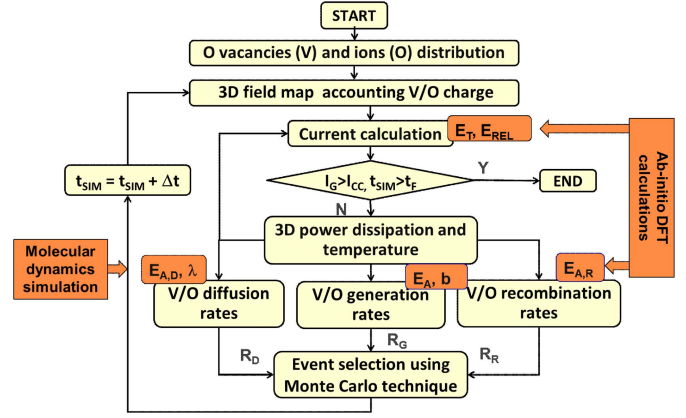

Fig. 1. Flowchart of the RRAM simulation model. t_{SIM} and t_F are the total and the maximum simulation time, respectively. I_G and I_{CC} are the gate and the compliance current, respectively. E_T and E_{REL} are oxygen vacancies thermal ionization and relaxation energies, whereas $E_{A,D}$, $E_{A,G}$, and $E_{A,R}$ are the activation energies of O vacancy/ion diffusion, generation, and recombination processes. b is the Hf-O bond polarization factor. The main parameters used in simulations are listed in Table I.

TABLE I
MAIN PARAMETERS USED IN SIMULATIONS

Symbol	DESCRIPTION	VALUE
$E_{REL}(\infty)$	relaxation energy of an isolated HfO$_x$ defect	1.19eV [14]
E_T	thermal ionization energy of HfO$_x$ defects	1.7-2.7eV [14]
r_t	HfO$_x$ defect radius	5.64Å
N_{CRIT}	critical defect density for the transition between TAT and drift conduction regimes	1.7·10^{22} cm^{-3} [36]
k	HfO$_x$ relative dielectric constant	21
k_{TH}	HfO$_x$ thermal conductivity	0.005 W/cmK [38]
υ	effective O-Hf bond vibration frequency	7·10^{13} Hz [15]
p_0	O-Hf bond polarization factor	5.2eÅ [15]
E_A	O-Hf bond breakage zero-field effective activation energy	2.9eV [15]
$E_{A,D}$	diffusion activation energy	vacancies: 1.5eV ions: 0.7eV [42]
$E_{A,R}$	recombination activation energy	0.2eV [43]

physical processes responsible for the RRAM operations, (i.e., defect-assisted electron transport, local power dissipation and temperature increase, stress-induced generation of oxygen and ions, and their diffusion and recombination) (Fig. 1).

The morphology of the polycrystalline HfO$_2$ is accounted for by considering a given number (depending on the total device area [19], [25]) of grains and GBs. Positively charged oxygen vacancies (which assist the TAT charge transport [11], [12], [15]) are distributed throughout both the grains and the GBs according to their atomic characteristics and densities [19]. The total current flowing through the device includes both the grain and the GB contributions. The electric field and potential profiles across the whole device volume are calculated by solving the Poisson equation in 3-D while accounting for the charge of both oxygen ions and vacancies. Coulomb repulsion (attraction) between species of the same (opposite) charge polarity is thus automatically accounted for. The calculation of the field accounts also for the local increase of the relative dielectric constant associated with the highly defective (metallic-like) oxide regions [26].

A. Charge Transport

The simulation of the current during the RRAM operations requires dealing with different conduction regimes ranging from the TAT to the DD.

In HfO$_2$ films, the TAT via oxygen vacancies is the dominant charge transport mechanism during forming and RESET [11], [12], [15], [27], [28]. We describe the TAT current in the framework of the multiphonon TAT theory [12], [14], [29] using the statistical kMC approach to account for the random distribution of oxygen vacancies in the oxide. The TAT current model accounts for the displacement of the lattice atoms surrounding the defect sites caused by charge trapping and emission events [30]. This lattice relaxation process depends on the atomistic structure of the defect. The relaxation energy, E_{REL}, a unique property of the defect controls the charge capture and emission processes and sets the temperature dependence of the TAT current [30], [31].

The traps assisting the electron transport in HfO$_2$ are associated with positively charged oxygen vacancies, V$^+$ [14], [16]. Using for the TAT defects the thermal ionization, E_T, and relaxation energies calculated through ab-initio methods for V$^+$ [32], we accurately reproduced the experimental currents measured across HfO$_2$-based stacks at different temperatures, indicating that the defects assisting the charge transport are properly identified [14], [15], [19], [25], [33].

Ab-initio calculations performed for MgO systems [34] have shown that the oxygen vacancy relaxation energy depends on their mutual distance, d, between the two defects involved in the charge transition. This phenomena occur in most of the oxide materials including HfO$_2$ [34] and can be described in the framework of the Marcus theory [35]. Here, we account for the reduction of E_{REL} with reducing the mutual distance between the defects through the Marcus-like relation

$$E_{REL}(d) = E_{REL}(\infty) \cdot \left(1 - \frac{r_t}{d}\right) \qquad (1)$$

where r_t is the defect radius, $E_{REL}(\infty) = S \cdot \hbar\omega_0$ is the relaxation energy of the isolated defect, S is the Huang Rhys factor [30], and $\hbar\omega_0 = 0.07$ eV is the phonon energy.

At very high O vacancy densities, typically reached at the final phases of the forming operation [11], [25], the charge transport is no longer dominated by the TAT, as the increased electron delocalization among adjacent defects leads to the formation of a defect subband. In these conditions, the dominant conduction mechanism is due to electron drift. The effective conductivity, which is still calculated in the TAT framework by neglecting tunneling and lattice relaxation contributions, whose probabilities are equal to one, approaches the value estimated experimentally [26] and theoretically according to the Landauer quantum conductance formula [36]. The critical defect density at which the drift becomes dominant was calculated using the density functional theory, $N_{CRIT} \approx 1.7 \times 10^{22}$ cm^{-3}, corresponding to an average defect-to-defect distance of 3.5 Å [37]. By accounting simultaneously for both the TAT and the drift, the model allows consistently reproducing the charge transport during the
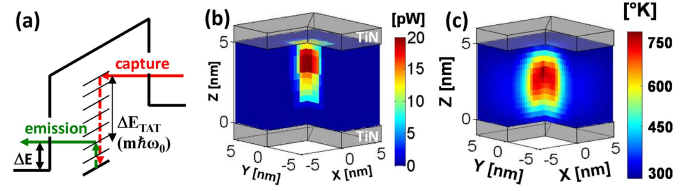

Fig. 2. (a) Schematic of the TAT process, where the net energy release occurring at the trap site is highlighted. (b) and (c) Corresponding 3-D power dissipation and temperature maps.

formation of metallic-like CF and the subsequent switching operations.

B. Calculation of Power Dissipation and Temperature Maps

The charge trapping taking place during the TAT is accompanied by a net energy release at the defect sites, whose entity depends on the misalignment between the electron energy and the ground state of the defect [Fig. 2(a)]. The associated power dissipation, which can locally increase the temperature, can be easily calculated through [25]

$$P_{TAT} = R \cdot \Delta E_{TAT} = R \cdot m \cdot \hbar\omega_0 \qquad (2)$$

where m is the net number of exchanged phonons and ΔE_{TAT} the released energy [Fig. 2(a)]. $R = (\tau_C + \tau_E)^{-1}$ is the rate of the electron flow, and τ_C and τ_E being the corresponding capture and emission times [14], [25], respectively. The power dissipated by carriers in the defect subbands inside the CF is calculated directly from the CF conductivity. The power dissipated at the anode due to the electron thermalization is given by $P_{AN} = R \cdot \Delta E$, where ΔE is the electron energy dissipated at the anode [25] [Fig. 2(a)]. The 3-D map of the power dissipated through the whole oxide, P, which includes the above contributions [Fig. 2(b)], is used to calculate the 3-D temperature profile, T, in the device by solving Fourier's heat flow equation [Fig. 2(c)]

$$P(x, y, z) = k_{TH} \cdot \nabla^2 T(x, y, z) \qquad (3)$$

k_{TH} is the thermal conductivity of the hafnium oxide [38].

C. Stress-Induced Generation of O Vacancies and Ions

The modeling of stress-induced generation of new oxygen vacancy/ion pairs (i.e., defects supporting the TAT) associated with the breakage of the Hf-O bonds is required to describe the structural modification occurring during forming and SET operations. The rate of the vacancy/ion generation is modeled in the framework of the thermochemical theory [15], [39]

$$G_F(x, y, z) = \upsilon \exp\left(-\frac{E_A - b \cdot F(x, y, z)}{k_B \cdot T(x, y, z)}\right) \qquad (4)$$

where F is the electric field, $\upsilon = 7 \times 10^{13}$ Hz is the effective vibration frequency of the O-Hf bonds [15], [25], k_B is Boltzmann's constant, $b = p_0 \cdot [(2+k)/3]$ is the bond polarization factor, where $p_0 = 5.2$ eÅ [15] and $k = 21$ are the HfO$_2$ molecular dipole moment [39] and relative dielectric constant, respectively. E_A is the zero-field effective

activation energy required to break the Hf-O bond, which depends on the atomic material characteristics. The value we considered, $E_A = 2.9$ eV, extracted from time-dependent dielectric breakdown measurements [15], is consistent with the substoichiometric hafnium oxide, i.e., HfOx used in the RRAM devices [11], [15].

D. Diffusion and Recombination of O Vacancies and Ions

The breakage of the Hf-O bond leads to the formation of an oxygen vacancy/ion Frenkel pair (O^{2-}, V^{2+}) [40]. Subsequently, the O ion can move in the surrounding lattice driven by electric field, temperature and concentration gradients (diffusion of oxygen vacancies is negligible due to the much higher diffusion barrier [41]). The diffusion and subsequent recombination of O ions and vacancies play a fundamental role in the RESET operation, which is believed to be due to the oxidation of the bottom portion of the CF operated by O ions back diffused from the top dielectric interface.

O^{2-} ions diffuse via interstitial positions [42]: the process, involving the substitution of O atom in the lattice network, is activated by the temperature and field, and its rate R_D is

$$R_D(x, y, z) = \nu \cdot \exp\left(-\frac{E_{A,D} - k_D \cdot F_{EFF}(x, y, z)}{k_B \cdot T(x, y, z)}\right). \quad (5)$$

$E_{A,D}$ is the activation energy, F_{EFF} is the electric field along the diffusion direction, and k_D is a factor (depending on atomic material properties) accounting for the field-induced energy barrier reduction. In simulations, we considered $E_{A,D} = 0.7$ eV and $E_{A,D} = 1.5$ eV for ions and vacancies [42], respectively. Due to the very high-energy barrier, V^{2+} do not diffuse during the RRAM operations, as confirmed by the monotonic trend of I_G—time curve typically observed during forming [12].

The ion/vacancy recombination rates are calculated using the same effective energy description

$$R_R(x, y, z) = \nu \cdot \exp\left(-\frac{E_{A,R}}{k_B \cdot T(x, y, z)}\right) \quad (6)$$

where $E_{A,R} = 0.2$ eV is the activation energy [43].

The O^{2-}/V^{2+} generation, diffusion, and recombination rates are consistently calculated in the oxide by considering the temperature and field maps accounting for the power dissipation and the oxygen ion/vacancy distributions (Fig. 2). A Monte Carlo technique is adopted to randomly select the event involving O^{2-} and V^{2+}, thus enabling statistical simulations. Every time a new diffusion/ recombination/generation event occurs, the field, the current and the related power dissipation, and the temperature are recalculated in the entire RRAM device volume. The simulation stops when either the current exceeds the predefined compliance (I_{CC}) limit or the simulation time reaches its maximum.

IV. DYNAMICS OF THE FORMING PROCESS

We used the model described in Section III to investigate the dynamics of the forming operation and its dependence on the external conditions.
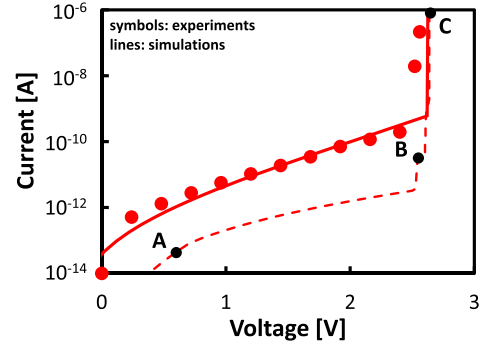

Fig. 3. Leakage current measured (symbols) and simulated (solid line) during an RVF on a 10-nm thick TiN/HfOx (10 nm)/Ti RRAM. Dashed line: contribution of the GB that is converted into the CF.
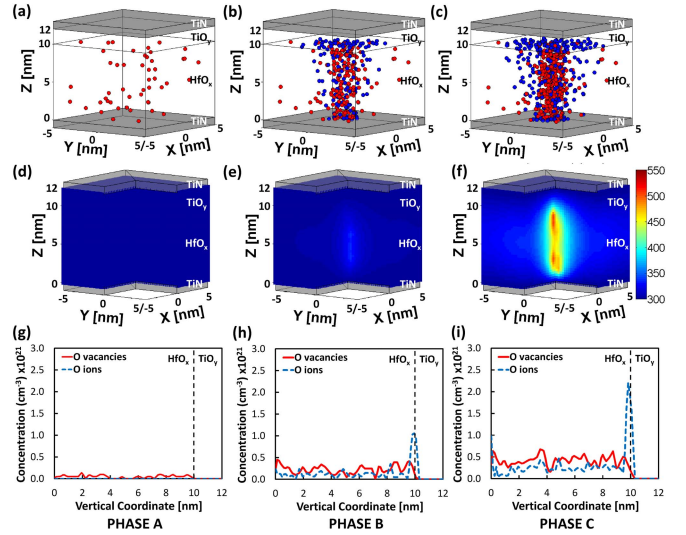

Fig. 4. Simulated (a)–(c) 3-D oxygen vacancy (red spheres) and ion (blue spheres) distributions, (d)–(f) 3-D temperature profile, and (g)–(i) average oxygen vacancy/ion densities around the CF at the phases A, B, and C of the forming transient, as shown in Fig. 3.

Fig. 3 shows the evolution of the currents measured and simulated on a 10-nm-thick TiN/HfO2/Ti/TiN RRAM device during a ramped voltage forming (RVF) with $I_{CC} = 1$ μA. The total current accounting for the contributions of every GB in the simulated device (solid line) reproduces the relatively slow increase of the experimental current until the abrupt current jump corresponding to the formation of the CF (Fig. 3). This abrupt current jump occurring at the forming voltage is due to the current flowing through the GB that is converted into the CF (see the dashed line in Fig. 3) consistent with the filamentary-type of conduction in HfOx-RRAM devices.

To gain insight into the dynamics of the forming process, we monitor the evolution of the GB that was converted into the CF as demonstrated by the RVF simulation in Fig. 3. Fig. 4 shows the evolution of both oxygen vacancy/ion distributions and the temperature profile at the subsequent phases of the forming transient, labeled as A, B, and C in Figs. 3 and 4. During the initial part of the forming voltage ramp (phase A) only few native defects are present in the GB [Fig. 4(a)]. Since they drive a relatively small current, the power dissipated at the GB is limited and the local temperature is

uniform and equal to the ambient one, as shown in Fig. 4(d). Moreover, the electric field across the oxide is relatively small ($V_G \ll V_{FORM}$), and therefore the probability to generate a new defect is very low and uniform across the entire RAM devices. Thus, few O vacancy defects are generated randomly throughout the RRAM HfO$_x$ volume without any correlation.

As the voltage approaches a certain critical value, V_{FORM} (phase B in Figs. 3 and 4), the higher electric field lowers the energy needed to break the Hf-O bond [see (4)] thus increasing the defect generation probability. However, the power dissipated within the GB remains still quite low. This leads to a small increase of the local temperature in the GB proximity, which translates into an almost uniform oxygen vacancy generation [Fig. 4(b)]. During this phase, the motion of the oxygen ions released by the Hf-O bond breakage is mainly controlled by the vertical electric field, since the radial movement, governed by local temperature and Coulomb repulsion, is limited. The negatively charged oxygen ions are thus driven by the electric field toward the top interface, where a TiO$_y$ layer has been formed during the fabrication process because of the O ion extraction (induced by the OEL) and the subsequent Ti oxidation [23]. Oxygen ions are shown to accumulate at the GB/TiO$_y$ interface, which could represent the so-called oxygen reservoir, ensuring the O ion supply for the subsequent switching operations [Fig. 4(b) and (h)]. Note that, once they reach the GB/TiO$_y$ interface, ions tend to spread laterally as a consequence of their mutual Coulomb repulsion.

A relevant change in the forming process dynamics occurs when the generated oxygen vacancy defects create a cluster [25], which strongly enhances the current and the temperature in the vicinity of the GB. This temperature increase further promotes the generation of new defects, triggering a thermally driven positive feedback that quickly leads to the formation of the CF ($V_G = V_{FORM}$, phase C in Fig. 4). During this final phase, the Hf-O bond breakage process becomes very fast, and the released O ions have less time to diffuse away in between two subsequent defect generation events. This leads to an accumulation of O ions in the close proximity of the CF [Fig. 4(c) and (i)]. The Coulomb repulsion between the O^{2-} ions and high local temperature promotes the radial migration of O ions [Fig. 4(c)]. The accumulation of oxygen ions around the CF increases their subsequent recombination with substoichiometric Hf in the CF that may increase the CF variability [21], [44]. This effect is more evident during the RVF with respect to the constant voltage forming (CVF) as discussed in Section V-B.

V. EFFECT OF FORMING CONDITIONS

In order to understand how forming conditions affect the properties of the CF, we simulated the forming operation as a function of temperature, stress mode [i.e., CVF, RVF, and pulsed voltage forming (PVF)], and current compliance.

Simulation results achieve on individual RRAM devices are used to understand the effect of forming conditions on the distributions of oxygen ions and vacancies. In these cases,
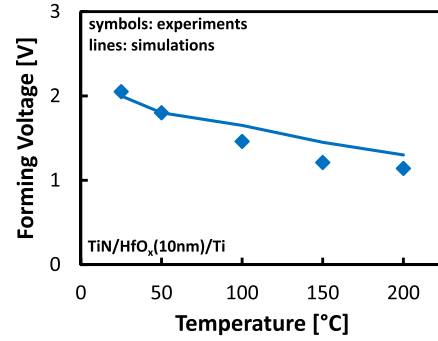

Fig. 5.   Forming voltage as a function of the external temperature (symbols) measured and (line) simulated on TiN/HfO$_x$ (10 nm)/Ti RRAMs.

simulations are stopped as soon as the compliance current is reached to identify the possible sources of variability and instability of the LRS associated with the O/V recombination.

We performed also a statistical simulation of the forming operation to investigate the forming condition effects on the LRS distributions. In this case, an additional relaxation time of ∼1 μs is considered after the current compliance is reached to account for the O/V recombination phenomena occurring at the end of forming, i.e., when the applied voltage drops and the internal temperature reduces to the equilibrium one.

A. Role of the External Temperature

Several studies have shown that external temperature (T_{EXT}) affects strongly the forming operation by reducing the forming voltage [45] and the LRS variability, and increasing the CF stability and reliability [44]. Fig. 5 shows the comparison between forming voltages, V_{FORM}, measured and simulated at different external temperatures. The simulations reproduce accurately the experimental V_{FORM} reduction with increasing T_{EXT}, which is due to the strong dependence of the Hf-O bond breakage process on the temperature (4). A higher forming temperature accelerates oxygen vacancy generation, consistent with the V_{FORM} reduction. The forming temperature affects also the movement of the oxygen ions released during the Hf-O bond breakage process, promoting their out-diffusion from the CF. As a consequence, increasing the temperature reduces the number of O ions remaining in close proximity of the CF at the end of the forming, as shown in Fig. 6(a)–(d). The subsequent recombination is strongly reduced, resulting into an increased CF stability [21], [44] and a reduced variability of the LRS resistance (R_{LRS}). It is worth underling that the external temperature acts as an accelerating factor of degradation and diffusion processes only until the onset of the thermal runaway leading to the formation of the CF. Once this positive-feedback process is triggered, charge transport, degradation, and diffusion are controlled by the local temperature in the CF, which exceeds by far the ambient one, with peak values higher than 1000 K.

Fig. 7 shows the R_{LRS} distributions measured and simulated at different temperatures after the RVF forming on a Ti/5-nm HfO$_x$/TiN RRAM devices by imposing a 1-μA current compliance. As expected, a higher T_{EXT} leads to a tighter R_{LRS} distribution, as shown in Fig. 7(a).
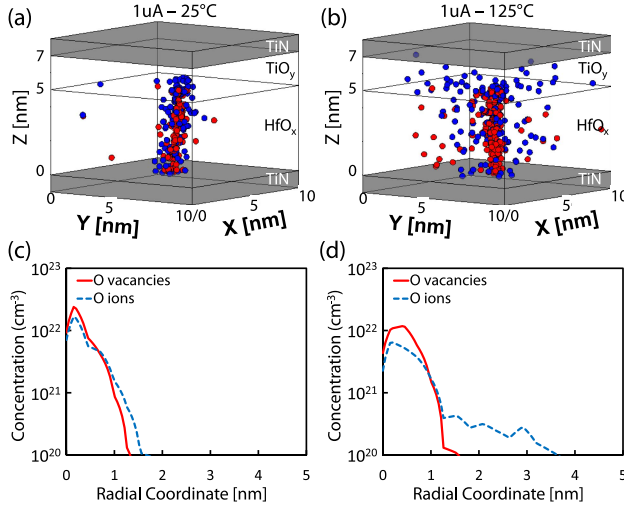
Fig. 6. Simulated (a) and (b) 3-D oxygen vacancy (red spheres) and ion (blue spheres) distributions and (c) and (d) 1-D oxygen vacancy/ion densities along the CF immediately at the end of RVF operations (i.e., as soon as the current compliance has been reached) performed at (a) and (c) 25 °C and (b) and (d) 125 °C, respectively. A current compliance of $I_{CC} = 1$ μA was imposed during the forming simulation.
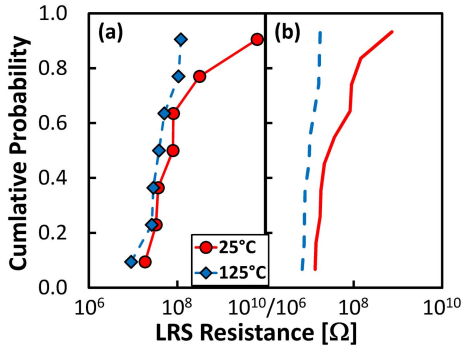

Fig. 7. (a) Experimental and (b) simulated cumulative distributions of the LRS resistances after the RVF forming performed at two different external temperatures $T_{EXT} = 25$ °C and 125 °C. The simulations of the LRS resistances are performed by considering an additional relaxation time of $\sim$1 μs after the current compliance (1 μA) has been reached.

This trend is accurately reproduced by the simulations [Fig. 7(b)] indicating that the temperature-enhanced O ions out-diffusion and reduced recombination are the reasons of the lower R_{LRS} variability.

B. Voltage Stress Mode

The characteristics of the CF (e.g., uniformity, O/V distributions, and so on) are significantly affected by the way the voltage is applied during forming, i.e., the CVF, the RVF, and the PVF.

In order to understand the effects of the forming voltage mode on the dynamics of the forming process and the CF characteristics, we simulated the forming operation on the same RRAM device under the CVF, the RVF, and the PVF regimes. Results show that the distribution of the oxygen ions is significantly affected by the voltage mode. In the CVF cases, O^{2-} ions accumulate mostly near the HfO$_x$/OEL interface, whereas they tend to distribute more
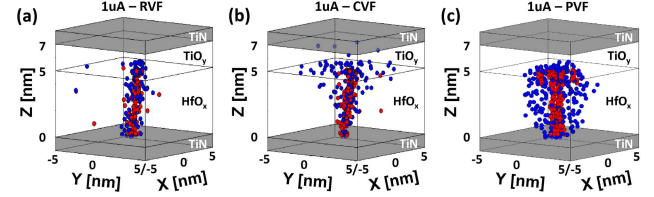

Fig. 8. Oxygen vacancy (red spheres) and ion (blue spheres) distributions obtained from simulations of (a) RVF, (b) CVF, and (c) PVF operations as soon as the current compliance has been reached. A 1-μA current compliance has been imposed during the forming simulation.

uniformly around the filament when forming is performed in both the RVF and the PVF. Conversely, the spatial distribution of oxygen vacancies is not affected by the voltage forming mode.

The differences in the ion distribution after the CVF, the RVF, and the PVF are related to the different role played by electric field and local temperature that control the vertical and the radial (random) components of O ion movement, respectively. In the CVF case, the relatively high electric field drives the O^{2-} ions toward the positively biased electrode. The time between two subsequent V/O generation events is much longer than that required for the ion to drift up to the top interface. Thus, ions do not mutually interfere in their diffusion, which is mostly controlled by the applied electric field. Conversely, in the PVF case, the application of a fast voltage pulse (whose amplitude exceeds V_{FORM}) increases exponentially the oxygen vacancy/ion generation rate. A very large number of oxygen ions is generated almost simultaneously and their subsequent diffusion is strongly affected by the Coulomb repulsion field due to O ions generated around the CF. This enhances the radial diffusion component determining a more dispersed O^{2-} distribution with respect to the RVF and the CVF [Fig. 8(c)].

C. Role of Current Compliance

The geometrical and physical characteristics of the CF are deeply affected by the current compliance imposed to limit the maximum current and power dissipation in the RRAM during forming. The current compliance allows to directly control the diameter of the CF [11]. Furthermore, it affects also the variability of the LRS resistance: increasing the current compliance allows reducing the R_{LRS} variability as can be seen in Fig. 9(a). This experimental trend is reproduced by the model simulations [Fig. 9(b)] showing a reduced average value and variability of the LRS resistance at increasing compliance limits. Simulations show that the reduction of the R_{LRS} variability is related to the higher density of oxygen vacancies generated at higher compliances, which leads to the formation of Hf-rich clusters (as discussed in Section III-A). The presence of these metallic-like clusters leads to a substantial redistribution of the electric field, which drops mostly across the less-defective CF oxide portions. This increases the generation rate of oxygen vacancies in the CF portion with the lower defect density, thus contributing to the CF uniformity and reducing R_{LRS} variability.
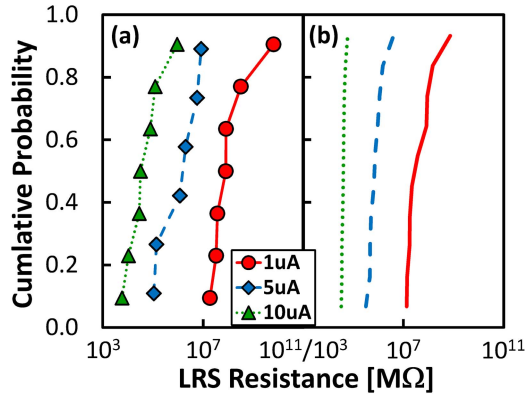
Fig. 9. Cumulative distributions of the LRS resistances (a) measured and (b) simulated as a function of the current compliance after the RVF at 25 °C on TiN/HfO$_x$ (5 nm)/Ti/TiN RRAMs. Simulations account for an additional relaxation time of $\sim$1 μs after the current compliance is reached.
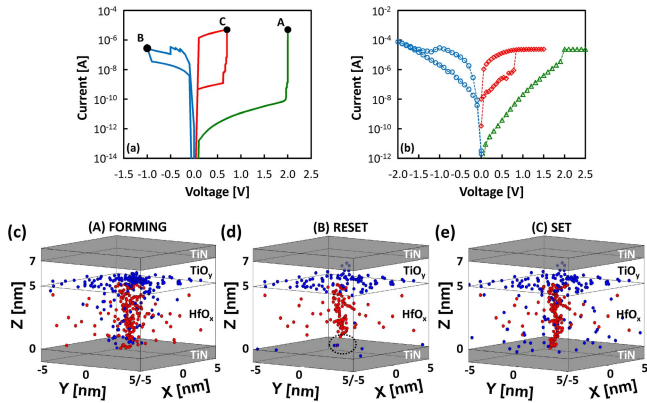

Fig. 10. Simulation of a forming-RESET–SET cycle with $I_{CC} = 5$ μA. I–V characteristics (a) simulated and (b) measured during a full forming-RESET–SET cycle (a 25-μA current compliance is imposed). 3-D oxygen vacancy (red spheres) and ion (blue spheres) distributions obtained from simulations at the end of (c) forming, (d) RESET, and (e) SET operations.

VI. SET AND RESET SIMULATIONS

The model is used to simulate SET and RESET (cycling) operations, starting from the CF obtained from the simulations of the forming process. No assumptions on the CF characteristics are made in the SET/RESET simulations, in contrast with other published models [4]–[9].

Fig. 10(a) shows the current–voltage characteristics simulated during forming and the subsequent RESET and SET operations, which reproduce the experimental I–V curves shown in Fig. 10(b): 1) the abrupt current increase at the forming voltage $\sim$2 V; 2) the gradual current reduction when applying the negative voltage sweep during RESET (that brings the device into the HRS); and 3) the subsequent abrupt current increase at $\sim$0.6 V during SET, which brings the device into the LRS. The model allows monitoring the evolution of the O vacancy and ion distributions during the operations. The oxygen ions accumulated at the top CF/TiO$_y$ interface during forming diffuse back toward the bottom HfO$_x$/TiN interface upon the application of the RESET negative voltage ramp [Fig. 10(c)]. During their diffusion, the oxygen ions can oxidized part of the CF before reaching the bottom electrode. However, since the voltage applied during

RESET has a relatively high amplitude (it is higher than the one applied during SET), the probability that the just formed Hf-O bonds can be broken again is very high. Thus, O ions have a high probability to be released again and to diffuse toward the bottom electrode pushed down by the electric field. When they reach the TiN diffusion barrier, they reoxidize the bottom tip of the CF, eventually forming a dielectric barrier [11] that is responsible of the current lowering associated to the LRS to the HRS transition [Fig. 10(d)]. All the microscopic phenomena qualitatively described above are accounted for in the framework of the model. This allows explaining also why during RESET a higher voltage (compared to SET) can be applied to the RRAM device without lowering the resistance to the LRS values, as happens during SET. The explanation of this voltage dilemma is related to the position of the dielectric barrier formed during RESET, close to the TiN electrode. Despite the relatively high voltage applied during RESET can break the Hf-O bonds, the diffusion of the released O ions is blocked by the TiN diffusion barrier and (laterally) by the other O ions due to Coulomb repulsion. The CF reoxidation is strongly favored by the high concentration of oxygen ions, which prevents the formation of the CF despite the high field/voltage applied.

Simulations show that the length of the dielectric barrier created at the bottom portion of the CF tip, which is typically within the 1–2-nm range [28], increases with the RESET voltage, consistently with the experimental data. Interestingly, simulations reproduce also the typical features of the RESET operation, i.e., the gradual current reduction after the voltage exceeds a threshold voltage of $\sim$−0.5 V [46], which is related to voltage magnitude required to promote the back-diffusion of the oxygen ions from the OEL reservoir down to the bottom.

Finally, applying the positive SET voltage ramp on the device in the HRS induces an abrupt current increase bringing the device back to the LRS, as shown in Fig. 10(b). This current jump is associated with the breakdown of the dielectric barrier created during RESET. The voltage applied to the device drops almost entirely across the barrier (due to the metallic nature of the remaining portion of the CF) and the electric field can exceed the critical breakdown field also at relatively low voltages. The HRS-to-LRS transition is thus governed by the field-enhanced generation of the defects in the dielectric barrier, which reconstructs the original (i.e., after forming) CF, bringing the device back to the LRS. The O ions released during the process diffuse toward the top oxygen reservoir where they accumulate [Fig. 10(e)] similarly to what happens during the initial forming operation.

VII. CONCLUSION

We presented a quantitative physic-based model for the operations of HfO$_2$-based RRAM linking the microscopic material properties and morphology to the device electrical characteristics. The model allows simulating all the RRAM operations in a unified and self-consistent framework, from the charge transport (accounting for the TAT-driven and ohmic-like conduction that are dominant in pristine and highly degraded dielectrics, respectively) to the degradation,

forming and the subsequent SET and RESET operations. The model has been used to investigate forming, SET and RESET dynamics, and the effect of operative conditions (temperature, voltage stress, and current compliance) on the microscopic changes occurring on the CF. Simulation results provide useful understanding of the physical processes governing the RRAM operations, crucial for device optimization and performance improvement.

REFERENCES

[1] H.-S. P. Wong *et al.*, "Metal–oxide RRAM," *Proc. IEEE*, vol. 100, no. 6, pp. 1951–1970, Jun. 2012.

[2] Y. S. Chen *et al.*, "Highly scalable hafnium oxide memory with improvements of resistive distribution and read disturb immunity," in *Proc. IEEE Int. Electron Devices Meeting*, Dec. 2009, pp. 1–4.

[3] A. Kalantarian *et al.*, "Controlling uniformity of RRAM characteristics through the forming process," in *Proc. IEEE Int. Rel. Phys. Symp.*, Apr. 2012, pp. 6C.4.1–6C.4.5.

[4] D. Ielmini, "Modeling the universal set/reset characteristics of bipolar RRAM by field- and temperature-driven filament growth," *IEEE Trans. Electron Devices*, vol. 58, no. 12, pp. 4309–4317, Dec. 2011.

[5] N. Raghavan, K. L. Pey, X. Wu, W. Liu, and M. Bosman, "Percolative model and thermodynamic analysis of oxygen-ion-mediated resistive switching," *IEEE Electron Device Lett.*, vol. 33, no. 4, pp. 712–714, May 2012.

[6] E. Miranda, D. Jiménez, and J. Suñé, "The quantum point-contact memristor," *IEEE Electron Device Lett.*, vol. 33, no. 10, pp. 1474–1476, Oct. 2012.

[7] S. Long *et al.*, "A model for the set statistics of RRAM inspired in the percolation model of oxide breakdown," *IEEE Electron Device Lett.*, vol. 34, no. 8, pp. 999–1001, Aug. 2013.

[8] S. C. Chae *et al.*, "Random circuit breaker network model for unipolar resistance switching," *Adv. Mater.*, vol. 20, no. 6, pp. 1154–1159, Mar. 2008.

[9] S. Yu, X. Guan, and H.-S. P. Wong, "Understanding metal oxide RRAM current overshoot and reliability using kinetic Monte Carlo simulation," in *Proc. IEEE Int. Electron Devices Meeting*, Dec. 2012, pp. 26.1.1–26.1.4.

[10] L. Vandelli, A. Padovani, L. Larcher, G. Bersuker, D. Gilmer, and P. Pavan, "Modeling of the forming operation in HfO$_2$-based resistive switching memories," in *Proc. 3rd IEEE Int. Memory Workshop*, May 2011, pp. 1–4.

[11] L. Vandelli *et al.*, "Comprehensive physical modeling of forming and switching operations in HfO$_2$ RRAM devices," in *Proc. IEEE Int. Electron Devices Meeting*, Dec. 2011, pp. 17.5.1–17.5.4.

[12] L. Larcher, A. Padovani, O. Pirrotta, L. Vandelli, and G. Bersuker, "Microscopic understanding and modeling of HfO$_2$ RRAM device physics," in *Proc. IEEE Int. Electron Devices Meeting*, Dec. 2012, pp. 20.1.1–20.1.4.

[13] A. Padovani *et al.*, "Statistical modeling of leakage currents through SiO$_2$/high-κ dielectrics stacks for non-volatile memory applications," in *Proc. IEEE Int. Rel. Phys. Symp.*, Apr./May 2008, pp. 616–620.

[14] L. Vandelli, A. Padovani, L. Larcher, R. G. Southwick, III, W. B. Knowlton, and G. Bersuker, "A physical model of the temperature dependence of the current through SiO$_2$/HfO$_2$ stacks," *IEEE Trans. Electron Devices*, vol. 58, no. 9, pp. 2878–2887, Sep. 2011.

[15] A. Padovani, L. Larcher, G. Bersuker, and P. Pavan, "Charge transport and degradation in HfO$_2$ and HfO$_x$ dielectrics," *IEEE Electron Device Lett.*, vol. 34, no. 5, pp. 680–682, May 2013.

[16] G. Bersuker *et al.*, "Grain boundary-driven leakage path formation in HfO$_2$ dielectrics," *Solid-State Electron.*, vols. 65–66, pp. 146–150, Nov./Dec. 2011.

[17] K. McKenna and A. Shluger, "The interaction of oxygen vacancies with grain boundaries in monoclinic HfO$_2$," *Appl. Phys. Lett.*, vol. 95, no. 22, p. 222111, 2009.

[18] V. Iglesias, M. Porti, M. Nafría, X. Aymerich, P. Dudek, and G. Bersuker, "Dielectric breakdown in polycrystalline hafnium oxide gate dielectrics investigated by conductive atomic force microscopy," *J. Vac. Sci. Technol. B*, vol. 29, no. 1, p. 01AB02, Jan. 2011.

[19] O. Pirrotta *et al.*, "Leakage current through the poly-crystalline HfO$_2$: Trap densities at grains and grain boundaries," *J. Appl. Phys.*, vol. 114, no. 13, p. 134503, 2013.

[20] M. Lanza, G. Bersuker, M. Porti, E. Miranda, M. Nafría, and X. Aymerich, "Resistive switching in hafnium dioxide layers: Local phenomenon at grain boundaries," *Appl. Phys. Lett.*, vol. 101, no. 19, p. 193502, 2012.

[21] B. Butcher *et al.*, "Modeling the effects of different forming conditions on RRAM conductive filament stability," in *Proc. 5th IEEE Int. Memory Workshop*, May 2013, pp. 52–55.

[22] K. G. Young-Fisher *et al.*, "Leakage current-forming voltage relation and oxygen gettering in HfO$_x$ RRAM devices," *IEEE Electron Device Lett.*, vol. 34, no. 6, pp. 750–752, Jun. 2013.

[23] M. Sowinska *et al.*, "Hard X-ray photoelectron spectroscopy study of the electroforming in Ti/HfO$_2$-based resistive switching structures," *Appl. Phys. Lett.*, vol. 100, p. 233509, 2012.

[24] A. Padovani, L. Larcher, P. Padovani, C. Cagli, and B. De Salvo, "Understanding the role of the Ti metal electrode on the forming of HfO$_2$-based RRAMs," in *Proc. 4th IEEE Int. Memory Workshop*, May 2012, pp. 1–4.

[25] L. Vandelli, A. Padovani, L. Larcher, and G. Bersuker, "Microscopic modeling of electrical stress-induced breakdown in poly-crystalline hafnium oxide dielectrics," *IEEE Trans. Electron Devices*, vol. 60, no. 5, pp. 1754–1762, May 2013.

[26] E. Hildebrandt, J. Kurian, M. M. Müller, T. Schroeder, H.-J. Kleebe, and L. Alff, "Controlled oxygen vacancy induced p-type conductivity in HfO$_{2-x}$ thin films," *Appl. Phys. Lett.*, vol. 99, p. 112902, 2011.

[27] F. M. Puglisi, L. Larcher, G. Bersuker, A. Padovani, and P. Pavan, "An empirical model for RRAM resistance in low- and high-resistance states," *IEEE Electron Device Lett.*, vol. 34, no. 3, pp. 387–389, Mar. 2013.

[28] L. Larcher, F. M. Puglisi, P. Pavan, A. Padovani, and G. Bersuker, "A compact model of program window in HfO$_x$ RRAM devices for conductive filament characteristics analysis," *IEEE Trans. Electron Devices*, vol. 61, no. 8, pp. 2668–2673, Aug. 2014.

[29] M. Zhang, Z. Huo, Z. Yu, J. Liu, and M. Liu, "Unification of three multiphonon trap-assisted tunneling mechanisms," *J. Appl. Phys.*, vol. 110, no. 11, p. 114108, 2011.

[30] K. Huang and A. Rhys, "Theory of light absorption and non-radiative transitions in *F*-centres," *Proc. Roy. Soc. London, A, Math. Phys. Sci.*, vol. 204, no. 1078, pp. 406–423, 1950.

[31] C. H. Henry and D. V. Lang, "Nonradiative capture and recombination by multiphonon emission in GaAs and GaP," *Phys. Rev. B*, vol. 15, no. 2, pp. 989–1016, 1977.

[32] D. M. Ramo, J. L. Gavartin, A. L. Shluger, and G. Bersuker, "Spectroscopic properties of oxygen vacancies in monoclinic HfO$_2$ calculated with periodic and embedded cluster density functional theory," *Phys. Rev. B*, vol. 75, p. 205336, May 2007.

[33] A. Padovani, N. Raghavan, L. Larcher, and K. L. Pey, "Identifying the first layer to fail in dual-layer SiO$_x$/HfSiON gate dielectric stacks," *IEEE Electron Device Lett.*, vol. 34, no. 10, pp. 1289–1291, Oct. 2013.

[34] K. P. McKenna and J. Blumberger, "Crossover from incoherent to coherent electron tunneling between defects in MgO," *Phys. Rev. B*, vol. 86, p. 245110, Dec. 2012.

[35] R. A. Marcus, "Electron transfer reactions in chemistry. Theory and experiment," *Rev. Modern Phys.*, vol. 65, pp. 599–610, Jul. 1993.

[36] R. Landauer, "Spatial variation of currents and fields due to localized scatterers in metallic conduction," *IBM J. Res. Develop.*, vol. 1, no. 3, pp. 223–231, 1957.

[37] J. Robertson and R. Gillen, "Defect densities inside the conductive filament of RRAMs," *Microelectron. Eng.*, vol. 109, pp. 208–210, Sep. 2013.

[38] M. A. Panzer *et al.*, "Thermal properties of ultrathin hafnium oxide gate dielectric films," *IEEE Electron Device Lett.*, vol. 30, no. 12, pp. 1269–1271, Dec. 2009.

[39] J. McPherson, J.-Y. Kim, A. Shanware, and H. Mogul, "Thermochemical description of dielectric breakdown in high dielectric constant materials," *Appl. Phys. Lett.*, vol. 82, no. 13, pp. 2121–2123, 2003.

[40] A. V. Chadwick, "Ionic conduction and diffusion in solids," in *Encyclopedia of Applied Physics*, vol. 8, G. L. Trigg, Ed. Berlin, Germany: Wiley, 1993.

[41] N. Capron, P. Broqvist, and A. Pasquarello, "Migration of oxygen vacancy in HfO$_2$ and across the HfO$_2$/SiO$_2$ interface: A first-principles investigation," *Appl. Phys. Lett.*, vol. 91, no. 19, p. 192905, 2007.

[42] A. S. Foster, A. L. Shluger, and R. M. Nieminen, "Mechanism of interstitial oxygen diffusion in hafnia," *Phys. Rev. Lett.*, vol. 89, no. 22, p. 225901, Nov. 2012.

[43] R. Govindaraj, C. S. Sundar, and R. Kesavamoorthy, "Atomic scale study of oxidation of hafnium: Formation of hafnium core and oxide shell," *J. Appl. Phys.*, vol. 100, no. 8, p. 084318, 2006.

[44] B. Butcher *et al.*, "Hot forming to improve memory window and uniformity of low-power HfO$_x$-based RRAMs," in *Proc. 4th IEEE Int. Memory Workshop*, May 2012, pp. 1–4.

[45] B. Traoré *et al.*, "Investigation of the role of electrodes on the retention performance of HfO$_x$ based RRAM cells by experiments, atomistic simulations and device physical modeling," in *Proc. IEEE Int. Rel. Phys. Symp.*, Apr. 2013, pp. 5E.2.1–5E.2.6.

[46] A. Fantini *et al.*, "Intrinsic switching variability in HfO$_2$ RRAM," in *Proc. 5th IEEE Int. Memory Workshop*, May 2012, pp. 30–33.

Andrea Padovani (S'06–M'10) received the Ph.D. degree from the University of Ferrara, Ferrara, Italy, in 2010.

He is currently a co-founder of MDLab s.r.l., Saint Christophe, Italy, a company developing electronic devices simulation software, and an Adjunct Professor with the University of Modena and Reggio Emilia, Modena, Italy. He works on the modeling of nonvolatile memories and logic transistors. He has co-authored over 100 technical papers.

Onofrio Pirrotta (S'13) was born in Reggio Calabria, Italy, in 1986. He received the master's degree in electronic engineering from the University of Calabria, Arcavacata di Rende, Italy in 2010, and the Ph.D. degree in industrial innovation engineering from the University of Modena and Reggio Emilia, Reggio Emilia, Italy, in 2015.

Luca Larcher received the Ph.D. degree in information engineering from the University of Modena and Reggio Emilia, Reggio Emilia, Italy, in 2001.

He is currently an Associate Professor with the University of Modena and Reggio Emilia. His current research interests include the characterization and physical modeling of non-volatile memory devices and charge transport in high-k dielectrics, and the design of CMOS integrated circuits for both communication and energy harvesting.

Luca Vandelli was born in Reggio Emilia, Italy, in 1985. He received the master's degree in electronic engineering and the Ph.D. degree from the University of Modena and Reggio Emilia, Reggio Emilia, in 2009 and 2012, respectively.

He currently holds a post-doctoral position with the University of Modena and Reggio Emilia.

Gennadi Bersuker focuses on the physical and electrical characterization, reliability and charge transport in multilayer materials stacks for applications in transistors, advanced memories, III–V logic, and 2D devices.

Mr. Bersuker is the Chair of the EDS Reliability Physics Committee and an Editor of the IEEE TRANSACTIONS ON DEVICE MATERIALS AND RELIABILITY.